Application of Cartesian Background Grid in combination with Chimera Method to predict Aerodynamics of Helicopter Fuselage

W. Khier, T. Schwarz

Institute of Aerodynamics and Flow Technology
German Aerospace Center (DLR)
Lilienthalplatz 7, 38108 Braunschweig, Germany

Abstract

Overlapping grid technique (Chimera) is combined with an automatically generated cartesian background grid to descretize the flow domain around a helicopter fuselage model. Three dimensional Navier-Stokes computations are performed with the DLR's CFD code FLOWer to predict air flow past an Eurocopter BO-105 fuselage under low Mach number forward flight conditions. The influence of several turbulence models of the two-equation $k - \omega$ type is analyzed via direct comparison with the measured pressure distributions and aerodynamic coefficients. Among the models considered, the SST model showed the best agreement with the experimental data.

1 Introduction

Air flow past helicopters ranks among the most complicated flows in industrial aerodynamics. This is mainly because helicopters operate under significantly different flying conditions, and consequently, various flow fields result around the aircraft. In addition, several interactional phenomena are caused by the rotary motion of the rotors. Depending on the conditions of flight, different schemes of aerodynamic interference may take place between the main rotor and the fuselage, as in hover, vertical flight, or slow advance cases. High speed forward flight involves interaction between the two rotors, where the tail rotor is contained, partially or totally, in the wake of the main rotor. Descend flight is another case where complex interaction also takes place. Besides the blockage effect of the fuselage, the main rotor, depending on the speed of descend, sinks inside its own wake. The situation is even more pronounced close to the ground, and the so called fountain effect increases the complexity of the flow.

With the increase in computer power witnessed recently, Computational Fluid Dynamics (CFD) has evolved as a research and development tool in aeronautic industry. The field of helicopters has been no exception, but owing to the complexity of the problem, recent research efforts concentrated on the individual elements of the aircraft. (1; 2; 3; 4; 5), for example, studied the flow around isolated rotors under various flight conditions, while (6; 7; 8) analyzed the flow around isolated fuselage. An attempt was made in (9; 10; 11) to study the rotor-fuselage interaction by both an actuator disc model and time accurate representation of the rotor's motion. Proper resolution in space and time proved, however, to be prohibitively expensive for the latter approach.

Generation of high quality structured grids around complex geometries is the most time and effort consuming step in the numerical simulation process. Overlapping grid techniques offer an attractive alternative to the classical multi block approach by breaking down complex configurations into a number of simple components, generating structured grids around each component individually, and interpolating the solution between the component grids during the solution process using a background grid which partially overlap them. However, proper overlap between the grids is essential for the stablity of the method. The interpolation of the data should take place far from high gradients (boundary layers, shocks,..etc.) otherwise the solution is contaminated by large interpolation errors, which may prevent the convergence of the solution. To guarantee accurate interpolation, the overlapping grids must have comparable resolutions within the overlap regions.

Satisfaction of the above conditions using one of the component grids (usually of the largest dimensions) as a background grid places additional constrains on grid generation, and may result in poor quality grids in many cases. In addition, considerable amount of time and effort is usually required before a moderate quality functioning Chimera grid can be obtained. Thus, Chimera application becomes less attractive in pratice when complex three dimensional configurations are involved, for which the technique is supposed to be most beneficial.

In this paper an alternative approach to transfer the data between the child grids is applied. The approach replaces conventional boundary fitted background grids by a cartesian grid. This approach has the following advantages. Firstly, a cartesian grid requires negligible human and computational effort. Secondly, identical grid resolutions can be achieved in the overlap regions. Thirdly, cartesian grids offer ideal numerical characteristics (no cross diffusion). Block local refinement is employed to ensure matching grid resolutions in the overlap zones only, thus keeping the number of grid points within acceptable limits.

Turbulence models based on the eddy viscosity hypothesis have become a standard tool in industrial CFD applications. In the helicopter field, the two-equation class of eddy viscosity models has gained recently increasing attention. Although their shortcomings, which can be easily deduced from their formulation, have been long known, they stand nowadays as a compromise between simple algebraic models (12) and one equation models (13) on the one hand, and the more accurate (and computationally expensive) differential stress models on the other hand. Motivated by their success, several attempts to minimize their deficiencies have been undertaken. However, since all statistical turbulence models are calibrated for simple flow cases, it seems logical to expect some inconsistency in their behavior when applied to different classes of flow, especially the complex ones.

The present paper demonstrates the potential of overlapping grid method (Chimera) in combination with cartesian background grid to generate the grid around a helicopter fuselage configuration. In addition, the performance of three models of the $k-\omega$ class in helicopter application is evaluated. The original Wilcox model (14) , the linear algebraic Reynolds Stress model of Rung (LEA) *et al.* (15), and the Shear Stress Transport (SST) model of Menter (16) are examined by comparison with experimental pressure distributions and force coefficients. Based on the outcome, the most accurate model is employed to predict the flow around the fuselage in different forward flight, low Mach number conditions. The governing equations are introduced in the first part of the following section, while the numerical method is highlighted in the second part. A description of the real geometry and flow conditions is given next. The numerical grids are described in the fourth section. The fifth section contains the numerical results and comparisons with experimental data. Conclusions drawn from the present investigation are summarized in the last section.

2 Governing Equations and Numerical Technique

Governing Equations. The integral for the time-dependent compressible Navier-Stokes equations written in relative reference frame reads

$$\frac{d}{dt}\int_{\mathcal{V}_r(t)} W_r\, dV_r + \int_{\partial\mathcal{V}_r(t)} \left(\bar{\bar{\mathsf{F}}}(W_r)\right)\cdot \vec{n}_r\, dS_r = 0 \tag{1}$$

where W_r is the vector of the conservative variables reads

$$W_r = \begin{pmatrix} \rho \\ \rho\vec{v}_r \\ \rho E \end{pmatrix} \tag{2}$$

Where density of a fluid particle is denoted by ρ, the specific total energy by E and the velocity vector by $\vec{v}_r$.

The specific total energy by E is related to the specific internal energy e by

$$E = e + \frac{1}{2}\vec{v}_r.\vec{v}_r \tag{3}$$

Finally, the flux density tensor is given by

$$\bar{\bar{\mathsf{F}}}(W_r) = \begin{pmatrix} \rho(\vec{v}_r)^t \\ \rho\vec{v}_r \cdot (\vec{v}_r)^t + p\bar{\bar{\mathsf{I}}}_3 - \bar{\bar{\tau}} \\ \rho E(\vec{v}_r)^t + p\vec{v}_r^t - (\bar{\bar{\tau}} \cdot \vec{v}_r)^t - \frac{c_p\mu}{\mathsf{Pr}}(\overrightarrow{\mathsf{grad}} T)^t \end{pmatrix} \tag{4}$$

where p, $\bar{\bar{\tau}}$, μ, T, c_p and Pr denote respectively the static pressure, the viscous stress tensor, the dynamic viscosity coefficient, the static temperature, the specific heat capacity at constant pressure and the Prandtl number.

This system of equations is closed by a perfect gas state law

$$p = (\gamma - 1)\rho e \tag{5}$$

where $\gamma = c_p/c_v = 1.4$ is the heat capacity ratio and the value of the Prandtl number typical of aircraft conditions is retained Pr $= 0.72$; and finally, the dynamic viscosity coefficient is calculated using Sutherland's formula

$$\mu(T) = \mu_S \left(\frac{T}{T_S}\right)^{3/2} \frac{T_S + 110.4K}{T + 110.4K} \quad (\mathsf{kg} \cdot \mathsf{m}^{-1} \cdot \mathsf{s}^{-1})\,. \tag{6}$$

Turbulence Modelling Turbulence effects are introduced using Boussinesq's eddy viscosity approach, which implies linear (Newtonian) stress-strain relationship. The eddy viscosity is estimated by Prandtl-Kolmogorov relation:

$$\mu_t/\rho = Vl \tag{7}$$

where V is a velocity scale and l is a length scale proportional to that of the energy-containing motions.

The velocity scale is usually taken equal to $k^{1/2}$. Numerous proposals have been made for establishing the proper length scale l (21; 22; 23; 24). For aeronautic applications the approach of Wilcox (14) (originally proposed by Kolmogorov) has proved superior to other two-equations eddy viscosity models. The Wilcox $k - \omega$ model computes the length scale as a function of the turbulence kinetic energy k and some scale determining quantity, ω, so that:

$$\mu_t = C_\mu \frac{\rho k}{\omega} \tag{8}$$

where ω is the specific turbulence dissipation rate (it can be interpreted physically as an eddy turnover frequency). Both k and ω are obtained via the following transport equations:

$$\left\{ \begin{array}{l} \dfrac{\partial \rho k}{\partial t} + \mathsf{div}\left(\rho k \vec{v}_r - \left(\mu + \dfrac{\mu_t}{\sigma_k}\right)\overrightarrow{\mathsf{grad}} k\right) = P_k - D_k \\ \dfrac{\partial \rho \omega}{\partial t} + \mathsf{div}\left(\rho \omega \vec{v}_r - \left(\mu + \dfrac{\mu_t}{\sigma_\omega}\right)\overrightarrow{\mathsf{grad}} \omega\right) = P_\omega - D_\omega \end{array} \right. \tag{9}$$

Two-equation models are known of their excessive production of eddy viscosity. This is a direct consequence of Boussinesq's assumption, which leads to positive production of the turbulence kinetic energy regardless of the state of strain. Thus, turbulence is produced by two-equation models equally by concave and convex curvatures, and by flow acceleration and deceleration. On the one hand, additional viscosity improves the robustness of computations, and on the other hand, is their major deficiency. Excessive turbulent mixing, for example, stabilizes boundary layers against adverse pressure gradients, delaying or completely preventing flow separation. Similarly, unsteadiness of the flow may also be suppressed for the same reason. Menter's SST model avoids partially this drawback by enforcing Bradshaw's assumption requiring the shear stress (in two dimensional cases) to be directly proportional to the kinetic energy of turbulence. This modifies the original expression of turbulent viscosity in Eq. 8, to:

$$\mu_t = \frac{1}{max(1, \frac{f_\mu \Omega}{0.3\Omega})} \frac{\rho k}{\omega} \tag{10}$$

where $f_\mu = tanh({a_2}^2)$ and $a_2 = max\left(\frac{2k^{0.5}}{\beta_k d_{min}\omega}, \frac{500\mu}{{d_{min}}^2 \rho\omega}\right)$. d_{min} is the minimum distance to solid wall.Ω is the absolute value of vorticiy $|\nabla \times \vec{v}|$.

In essence, the model switches between the turbulent time scale provided by ω and another time scale proportional to a mean flow quantity, Ω, scaled by a suitable detector of the wall vicinity. By choosing the minimum of the two scales, the model limits the eddy viscosity thus reducing the previously mentioned shortcoming of two-equation models.

LEA model (15) follows another route to overcome the problem. Assuming equilibrium between production, dissipation and redistribution of Reynolds stresses, a nonlinear expression for the stress anisotropy tensor as a function of strain and vorticity tensors can be derived. However, only the linear part of the stress-strain relation is retained in the present implementation due to numerical stability reasons. Thus, our version of LEA differs from standard Wilcox model only in the definition of C_μ, which takes the following form instead of a constant value.

$$C_\mu = \frac{\beta_1}{1 - \frac{2}{3\eta^2} + 2\xi^2} \tag{11}$$

where η and ξ are functions of strain and vorticity tensors, and turbulent production and dissipation according to (15).

To conclude, the full set of clsoure coefficients is shown in table 1. The values are slightly different from the orginial given in (14),(15),(16).

Model	C_μ	β_k	$\beta_{\omega 1}$	$\beta_{\omega 2}$	σ_k	σ_ω
Wilcox	1.0	0.09	0.555556	0.71	2.0	2.0
SST	$\frac{1}{max(1, \frac{f_\mu \Omega}{0.3\Omega})}$	0.09	0.555556	0.71	2.0	2.0
LEA	$\frac{\beta_1}{1-\frac{2}{3\eta^2}+2\xi^2}$	0.09	0.555556	0.71	2.0	2.0

Table 1: Closure coefficients used in the present paper.

Numerical Approach The previous equations are solved by means of the CFD simulation code FLOWer developed at DLR since the beginning of the 90's. The solution process is based on Jameson's method (29) where a second order central scheme is used for the discretization of the fluxes. A stabilizing blend of second and fourth order dissipation is added to the convective fluxes of the main flow equations, and a first order accurate Roe's scheme is employed to compute the turbulent convective fluxes.

The descretized equations are advanced in a fictitious time using a multi-stage Runge-Kutta method. The solution process makes use of acceleration techniques like local time stepping, multigrid and implicit residual smoothing. Turbulence transport equations are integrated over pseudo-time implicitly. Each (pseudo) time step, a system of equations is solved by the DDADI (diagonal dominant alternating direction implicit) to obtain k and ω.

No-slip and farfield (one-dimensional characteristic theory) boundary conditions for the mean flow equations are set respectively on solid bodies, and on remote surfaces.

No assumptions are made for the boundary layer profile, rather, the equations of motion are integrated down to the wall (Low-Re approach). On solid surfaces, the turbulence kinetic energy k is set equal to zero, and the specific dissipation rate ω is obtained from the equilibrium between dissipation and diffusion of ω in the viscous sub-layer, leading to $\omega = \frac{6\mu}{\beta_{\omega 2}\rho y^2}$ on the wall.

Chimera Method The Chimera implementation in the FLOWer flow solver can be split into three parts: 1) the hole cutting procedure, 2) the establishment of the intergrid communication and 3) the data transfer during the solution process.

Within the hole cutting phase all grid points which are inside of a solid body are flagged to be excluded from the flow calculation. The flagged grid areas are often called 'hole'. The test if a point is inside or outside of a body may be very CPU time consuming if it is based on the original body geometry. Therefore, FLOWer expects a user input providing one or more additional grids, which approximate the body volume by using only a small number of grid cells (usually 1 - 1000). The approximate body grids must totally enclose the solid body. Now all grid points representing the body are supposed to lie within the approximate body grid. Due to the small number of grid cells, this test is very fast.

After the holes are cut, FLOWer generates a list of points for which data must be interpolated from other grids. This includes the points at grid boundaries with Chimera boundary condition and the points located at the artificial boundaries around holes. Now for each interpolation point all other grids are searched for donor cells which may be used to interpolate flow data from. The search uses an alternating digital tree (ADT) search algorithm (27) in case of a general mesh and a specialized fast method for cartesian grids. If more than one grid overlaps the interpolation point, the data are interpolated from the cell with the smallest cell volume since this cell is assumed to give the most accurate flow representation. The donor cell is subdivided into six tetrahedrons to calculate the interpolation coefficients for trilinear interpolation.

If two grids overlap on a body surface, the body surface is not uniquely defined any more due to the different cell size of the grids at the body surface. This usually leads to an inaccurate interpolation especially if there are high flow gradients near the wall e. g. a boundary layer. To overcome this problem, FLOWer uses a correction method based on the ideas presented in (26).

The hole cutting phase and the search procedure are preprocessing steps which are required only once in case of a steady flow calculation.

The information on the holes and interpolation coefficients are now used to calculate the flow on the Chimera grid system. Grid points with Chimera boundary condition are updated by interpolating the conservative variables from the corresponding donor cells. In case of a multigrid computation, the interpolation of data is carried out on the finest grid level only. On coarser grid levels, the points at Chimera boundaries are updated with flow data from the finer level of the same grid. FLOWer allows to use any turbulence model in combination with the Chimera method.

3 Test Cases

The computations reported here simulate four test cases selected out of a series of wind tunnel tests carried out on a scale model of an EC BO-105 (originally MBB BO-105) helicopter. The BO-105 (Fig. 1.a), which has been introduced in the late sixties, is a twin engine, light weight, multi mission, hinge less rotor helicopter that has been used for a wide range of applications like passenger transport, search & rescue and law enforcement service. Figure 1.b shows the model mounted on model support inside the German-Dutch wind tunnel (DNW). A full description of the test stand and its main components is given in (17).

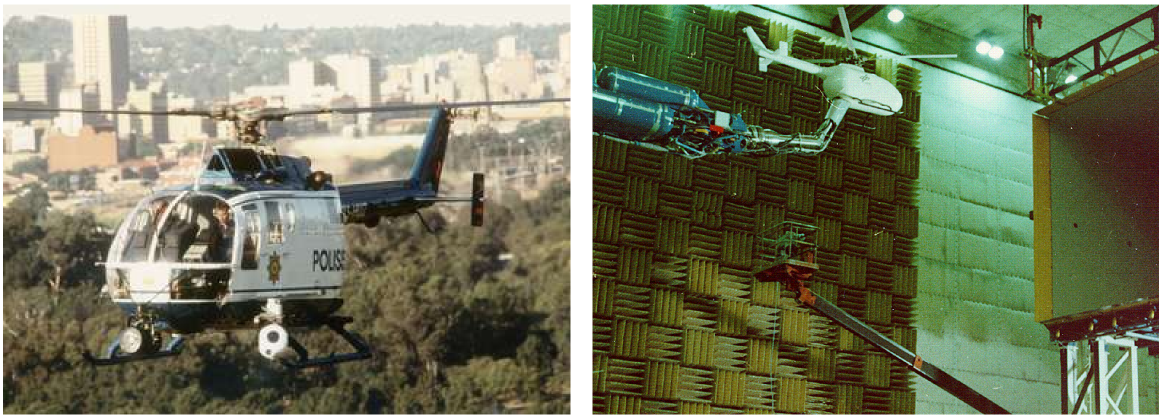

a) *b)*

Figure 1: *a)* EC BO-105 helicopter, *b)* The experimental setup

The measurements included both isolated fuselage and fuselage-rotor configurations under a wide variety of flight conditions. Hover as well as forward flight tests were included for speeds up to $46.5m/sec$, and a tip Mach number equal to 0.641. Four test facilities were used to assess the effect of the blocking ratio and other tunnel related factors under different pitch angles. The test procedure and results are reported in (18), (19) and (20). Table 2 contains a description of the selected test cases.

Test Case	α	Re	Ma_∞
TC-1	8.17^o	8.51×10^6	0.136
TC-2	3.14^o	8.51×10^6	0.136
TC-3	-1.87^o	8.51×10^6	0.136
TC-4	-6.94^o	8.51×10^6	0.136

Table 2: Test Matrix. α the pitch angle in degrees

4 Geometrical Characteristics and Grid Generation

As the actual wind tunnel model, all surface details of the real helicopter were excluded from the computations. Only those components of the fuselage with major aerodynamic function were retained, namely, the spoiler and horizontal stabilizer. The computational model included a simplified model support of equal dimensions to that used in the experiment. This was based on earlier experience which revealed strong blocking effect on the lower side due to the strut. Figure 3 shows clearly the rise in pressure on the lower surface of the fuselage. The pressure distribution on the upper surface is not affected by its presence.

The different components were distributed in four groups: naked fuselage, left stabilizer, right stabilizer, and strut and spoiler. Conventional multi-block structured grids were generated around each group individually by trilinear interpolation. Elliptic smoothing was applied subsequently to improve grid quality. The component grids consist of 45 blocks (Fuselage: 22, Strut+Spoiler: 9, left and right stabilizers: 7 each) and a total number of 4.27 Million point. The background grid consisted of 301 blocks and 1.56 Million points.Figure 4 shows the numerical grid used. The figure demonstrates clearly the potential benifits of the cartesian background grid approach. This is can be most clearly seen in the overlap region where the resoultion of the background grid is adapted to the resoultion of the child grids.

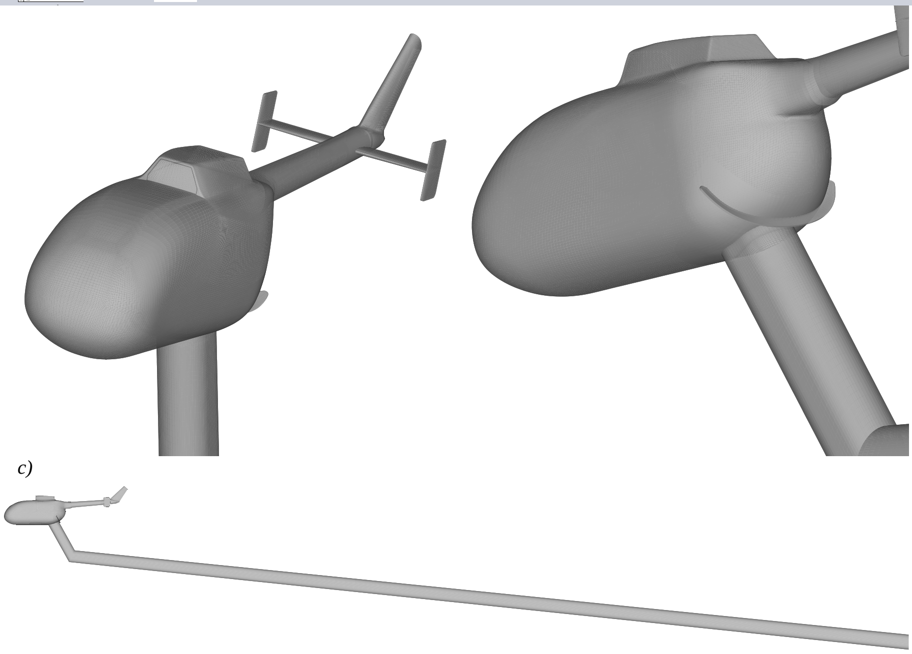

Figure 2: Geometry of the computational model, a: front view, b: rear view showing the spoiler and strut-fuselage connection, c: side view showing the extension of the flow domain downstream of the fuselage

Cartesian grid generator for Chimera background grid Cartesian grids have been successfully used to solve Euler equations around complex configurations. The method has gained a considerable atention in CFD because cartesian grids can be easily generated around arbiterarily complex geometries requiring only negligible human and computational efforts (33), (34). When Navier-Stokes simulation is considered, special treatement of the near wall region is necessary, otherwise a prohibitively large number of points is needed to resolve the boundary layer by uniform,low aspect ratio cells.

One way to overcome the above mentioned disadvantage is to combine Chimera with cartesian grids to generate computational grids for viscous computations. Conventional Chimera child grids are generated in the regions close to the individual components, and an automatically generated cartesian grid serves as a background grid as shown by Meakin (31). Hence, the advantages of both techniques can be exploited

The grid generator used in this paper allows to automatically create cartesian background grids which are adapted to the size of the cells in the nearfield grids. Anisotropic refinement (non cubic cells) is used to increase the similarity of the cells in the overlap region to reduce interpolation errors. The anisotropic refinement also significantly reduces the number of cells required for the background grids. Due to the grid overlap, the calculation of cut cells for the cartesian cells is not necessary. This simplifies the development of a cartesian grid generator significantly. Since FLOWer is a block structured code, the grid generator does not create individual grid cells but small grid blocks with a user given number of cells in each index direction. A typical block size is 8x8x8 cells. The grid generator stores all grid data in an ADT-tree. This ensures a fast access to all data during the grid creation process and sets no limitations related to anisotropic refinement. Other cartesian grid generators store data in Octrees, which makes extension for anisotropic cells difficult.

The resulting background grid may have up to 10000 grid blocks. The number of grid blocks is reduced by a subsequent merging procedure. Here the method of the weakest descent proposed by Rigby (32) is used to merge as many adjacent grid blocks as possible. This usually reduces the number of grid blocks by a factor of ten. The time needed for block merging is of the same order of the time needed to create the grid itself. The grid creation and the merging process run without user interaction.

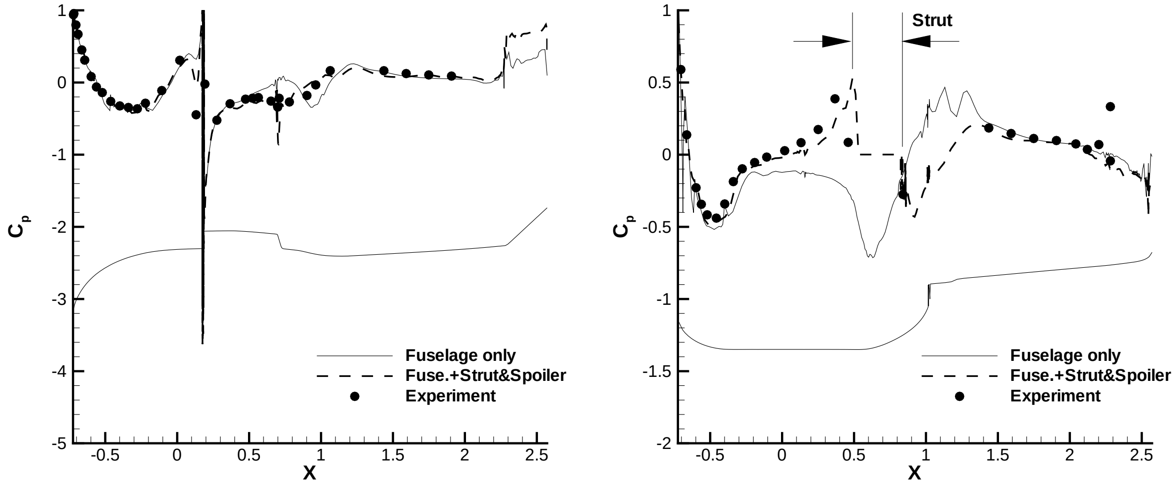

Upper surface *Lower surface*

Figure 3: Comparison between computed and measured pressures at symmetry plane, TC-2:$\alpha = 3.14^o$

5 Numerical Results

Pressure coefficient distribution at symmetry is shown in figure 5 for case TC-2. The figure compares computed results obtained by Wilcox, LEA and SST with the experimental values. On the upper surface, the three models behave similarly in the nose region. Marching downstream, Wilcox model begins to depart from the other two predicting higher pressure in front of the engine fairing. While LEA and SST behave in an opposite sense in this area, all three models deviate almost equally from the experiment. It is not quite clear which model behaves better on the leading upper edge of the engine fairing as there is no sufficient experimental data to evaluate the suction peaks predicted by the three models. The lowest pressure is predicted by SST equal to -4.1 followed by LEA showing a C_p value of -3.6. Wilcox model recovers the pressure slower than LEA and SST models on the engine fairing probably because larger flow separation on the upper surface. Further downstream, no significant differences between the models can be observed, and the three models show fairly good agreement with the experiment. On the lower surface, the three models show comparable accuracy upstream of the strut. Noticeable differences can be seen only in the immediate vicinity of the strut, where higher pressure is predicted by Wilcox's model. No experimental data is available for the region downstream of the strut and up to one third of the tail boom. Within this region, Wilcox model deviates considerably from the other two models predicting higher pressure (and possibly higher lift). A similar situation as on the upper surface is observed along the tail boom. All three models show almost equal deviation from experiment but with different trends: Wilcox model overestimates the pressure whereas the other two underestimate it.

The above guess is confirmed by the friction contours shown on figure 6. Wilcox model indeed produces a larger separation zone on the top of the engine fairing, corresponding to the observed slow pressure recovery in that region.

All three models predict more or less the same contribution of the strut to the aerodynamic forces as shown in table 3. SST results indicated the lowest influence of the strut, where as Wilcox model revealed the strongest contribution. The variation in contributions among the models is, however, negligible.

The presence of the strut is essential for the development of the flow under the fuselage, but the resulting forces acting on it are of no importance in the present investigation. Therefore, the strut

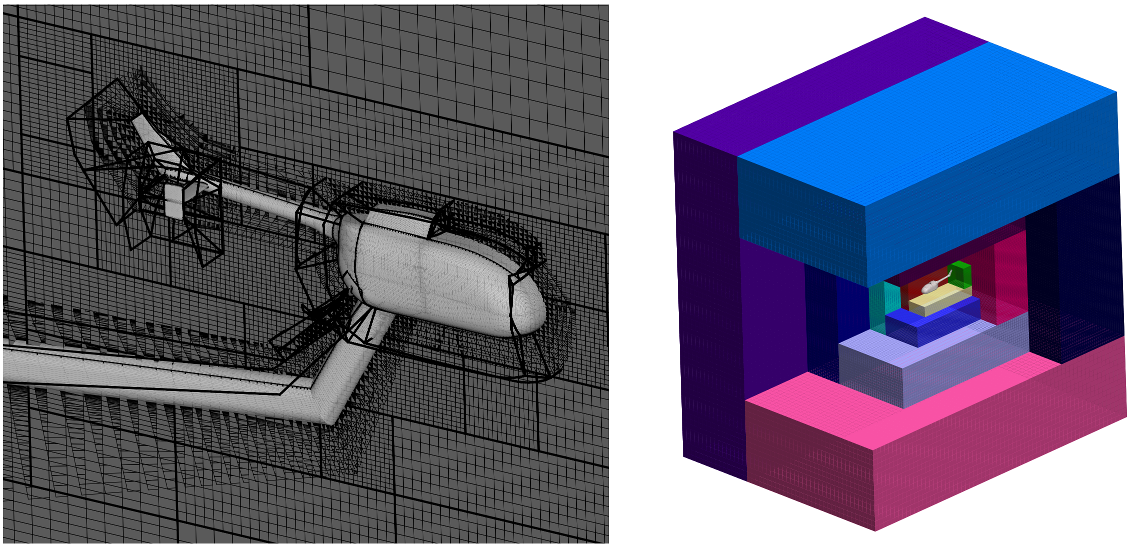

(b (a

Figure 4: A view of the numerical grid employed in this paper. a) Cross sectional view of the background grid showing the refinement of the grid close to the component grids indicated in thefigure by their outer boundaries. b) A global view of the computational domain showing the arrangement of blocks around the fuselage.

	LEA	*SST*	*Wilcox*
Lift (%)	89.7	89.2	90.3
Drag (%)	53.01	52.3	53.7

Table 3: Contribution of the strut to total drag and lift

will be excluded in the analysis of the aerodynamic forces presented hereafter. Tables 4 and 5 list in percentage the aerodynamic drag and lift acting on each component. It is interesting to see that both LEA and SST result in a strikingly close drag breakdown. The discrepancy in drag between the two models is less than 0.1%. Wilcox model predict similar contributions but the values differ with about 3% from LEA and SST.

	LEA	*SST*	*Wilcox*
Fuselage (%)	93.28	93.28	90.35
Left Stabillizer (%)	1.81	1.75	2.79
Right Stabillizer (%)	1.82	1.78	2.77
Spoiler (%)	3.09	3.19	4.09

Table 4: Drag breakdown - Test case TC-2

Different trends are observed for the aerodynamic lift. The maximum and minimum contributions of the fuselage vary by about 16.5%. All three models predict significant differences between left and right stabilizers. LEA and SST show higher lift acting on the right stabilizer than the left one, while Wilcox model predicts an opposite trend and smaller difference between the two components.

Viscous drag ranges from 8.52% and 10.11% of the total drag acting on the fuselage as shown in table 6. Regardless of the model used, viscous effects are below 2% for the other components. The contribution of viscous terms to lift is even less significant.

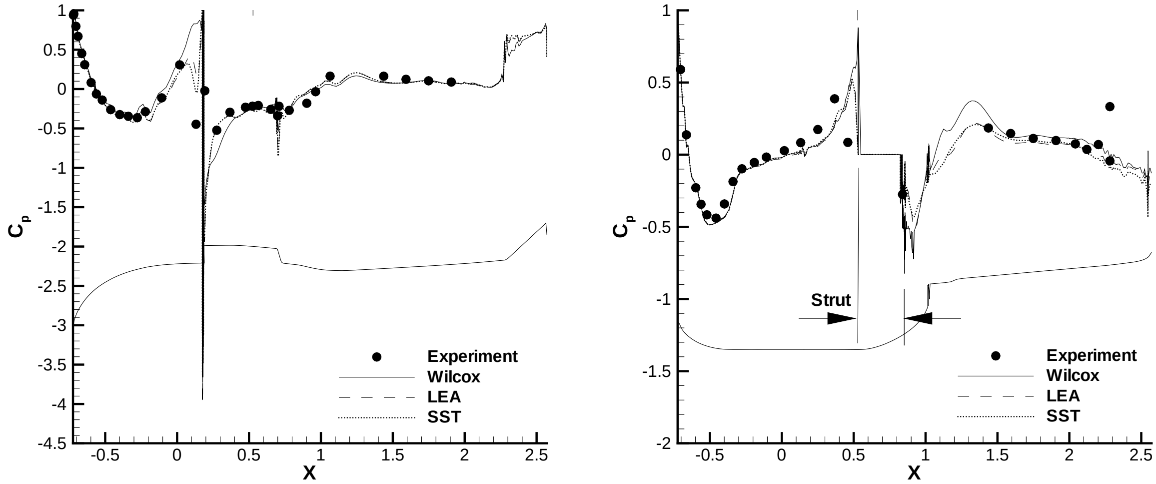

Upper surface *Lower surface*

Figure 5: Comparison between computed and measured pressures at symmetry plane, TC-2:$\alpha = 3.14^o$

	LEA	*SST*	*Wilcox*
Fuselage (%)	86.81	94.26	78.70
Left Stabillizer (%)	4.25	1.38	10.78
Right Stabillizer (%)	8.05	2.91	8.63
Spoiler (%)	0.90	1.46	1.90

Table 5: Lift breakdown - Test case TC-2

	LEA	*SST*	*Wilcox*
Fuselage (%)	9.83%	8.52%	10.11%
Left Stabillizer (%)	1.81%	1.61%	1.16%
Right Stabillizer (%)	1.88%	1.66%	1.22%
Spoiler (%)	−0.03%	−0.05%	−0.02%

Table 6: Viscous drag contribution

Finally the computed coefficients are compared to their experimental counterparts in table 7. Despite similarities in behavior observed previously, LEA model deviates from SST predicting drag and lift coefficients close to Wilcox results. SST shows the best agreement with experiment for this flight conditions and will be retained therefore as the standard model for the rest of the investigation.

	LEA	*SST*	*Wilcox*	*Experiment*
C_d	0.3964	0.4240	0.3957	0.495
C_l	0.177	0.205	0.169	0.235

Table 7: Computed and measured force coefficients for $\alpha = 3.14^o$

The computed and measured lift and drag coefficients are compared in figure 7.a. As can be seen from the figure, both the lift and the drag increase with the pitch angle. The computations reproduced that trend for both force components. However, the computed drag value is underestimated for the whole range of α. The deviation in drag ranges between 14.9% and 17.80 %, and corresponds to

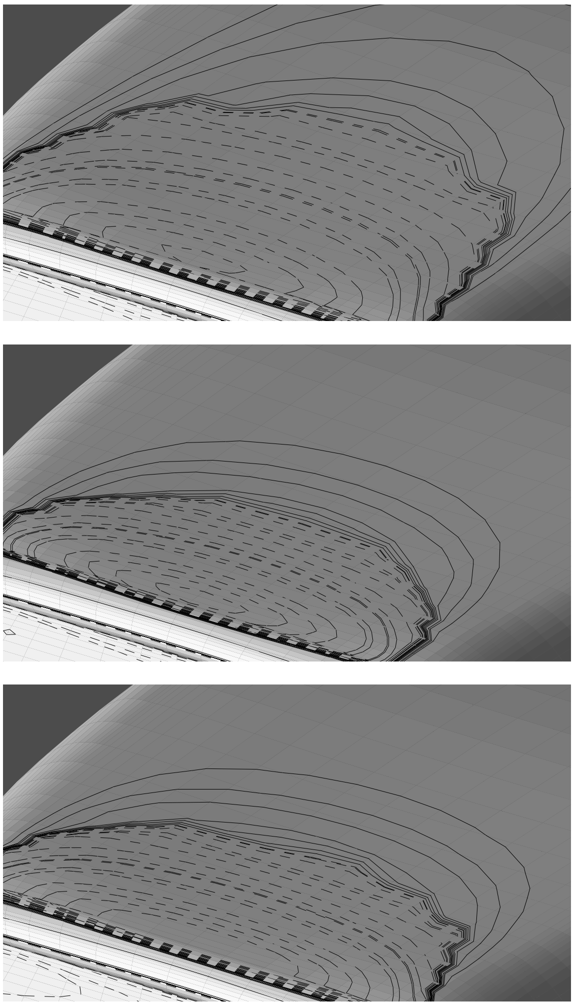

Wilcox

LEA

SST

Figure 6: Trace of the separation on the top of the engine fairing represented by friction coefficient contours. Solid and dashed lines denote postive and negative friction coefficient respectively

pitch angle equal to -1.87^o and 8.17^o, respectively. The computed lift shows a different trend than the experimental one, overestimating the lift force at α = -1.87^o, showing the best agreement with the experiment at α between 1.87^o and 3.14^o. then deviating again predicting lower value than the experiment as α increases. The most significant deviation was noticed for the α = 8.17^o. The α = -1.87^o case showed a slightly better agreement.

An alternative way to interpret the results is provided by the polar shown in figure 7.b. The computations consistently underestimate the drag for a given lift value. The trend, however, is well reproduced, where higher lift is associated with an increase in the drag. The rate of change of lift with respect to drag (the slope of the curve) is remarkably well predicted.

Figure 8 shows the computed pressure coefficient distribution at symmetry plane for the four pitch angles. As far as the qualitative character of the results is concerned, the surface pressure patterns on the upper side does not depend on the pitch angle except in the region downstream of the engine fairing. On the lower side the pressure distribution shows more or less the same trend for all pitch angles. Good agreement between the computations and experiment can be observed. The compu-

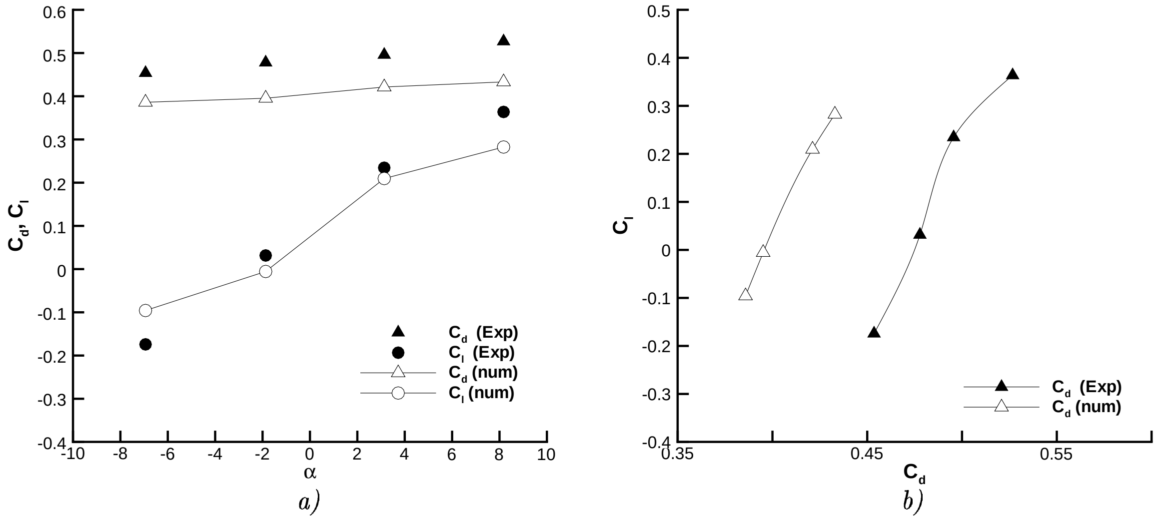

Figure 7: Comparison of SST results and experimental force coefficients: a) Drag and lift coefficients as function of pitch angle, b) Computed and measured aerodynamic force polars

tations captures the flow acceleration on the leading end and stagnation effect of the strut reasonably well. The latter, however, is characterized by a slight delay in pressure rise close to the strut. The same also applies to the engine casing on the upper side where the deviation from the experimental values becomes clear as the casing is approached. The wake of the engine casing turned out to be the most critical region of the flow. In that region, the computations failed to adequately predict the pressure distribution for the smallest and largest pitch angles. For the intermediate cases, the pressure intensity is predicted reasonably good, but its shape does not conform with the experiment. The observed pressure pattern denotes a closed separation bubble where the pressure increase represents the reattachment location. This well known deficiency of two equation turbulence models, that is, the inability to predict three dimensional separation adequately–seems to prevail despite the SST modifications.

6 Conclusions

Three dimensional Navier-Stokes computations around an isolated BO-105 fuselage have been presented. Chimera overlapping grid technique has been used to facilitate grid generation. A Cartesian, locally refined grid enclosed the component grids. The background grid was refined in such a way to ensure proper overlapping automatically without user's input. The outcome was a dramatic reduction of the effort required to start Chimera computations using conventional grids. A preliminary investigation has been performed to compare different variants of the $k - \omega$ model. Detailed analysis of the results has been carried out, which included pressure distribution and aerodynamic force comparisons with the experiment. All three models predicted similar drag breakdown, while SST predicted the highest contribution of the fuselage unit (without the strut, spoiler and stabilizers) to aerodynamic lift. The analysis revealed superior performance of Menter's SST model to predict aerodynamic forces. However, when other pitch angles were considered, the agreements between SST results and the experiment deteriorated, especially for the largest and smallest pitch angles. The strongest discrepancy between experimental and computed pressure was observed downstream of the engine casing, where SST fails to predict the pressure accurately, presumably due to incorrect prediction of the reattachment location. This behavior seems inline with previous observations, and probably due to a classical shortcoming of two equation models to predict complex three dimensional flow separation with reattachment. However, in view of the complexity of the flow and scarcity of detailed experimental data, this statement remains without a proof.

Acknowledgment This work is partially funded Eurocopter Deutschland. The authors would like also to thank Mr. B. Junker and H.J. Langer of The Institute of Flight Systems, DLR for their help in processing the experimental data.

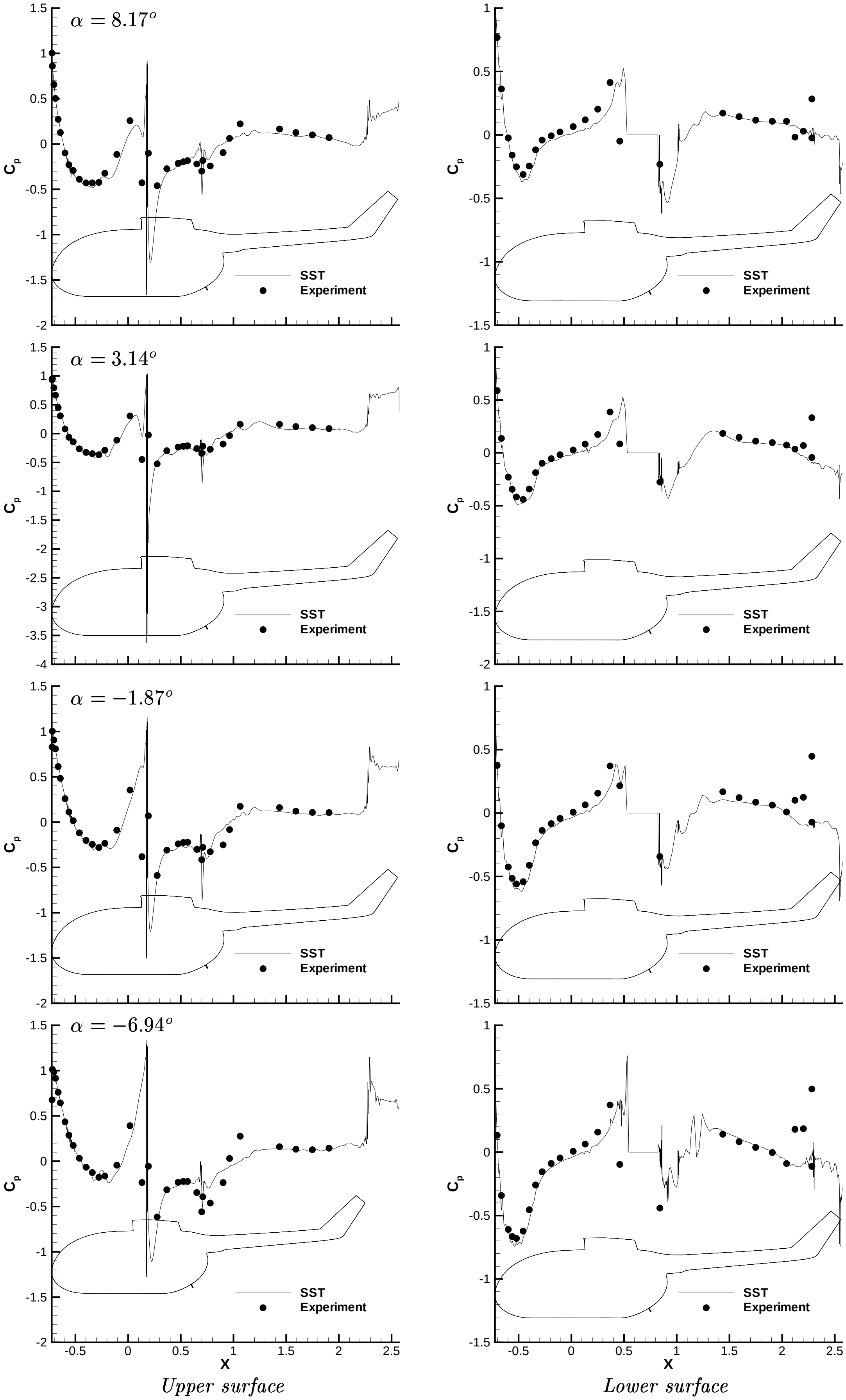

Figure 8: Pressure coefficient distribution at symmetry plane as a function of pitch angle

References

[1] P. Beaumier, E. Chelli, K. Pahlke: *Navier-Stokes Prediction of Helicopter Rotor Performance in Hover Including Aero-Elastic Effects*, American Helicopter Society 56^{th} Annual Forum, Virginia Beach, Virginia, May 2-4, 2000.

[2] E. Chelli, K. Pahlke: *Calculation of Viscous Flow Around the BO105 Main Rotor in Hover*, DLR Internal Report IB-NR 129-99/27.

[3] K. Pahlke, B. van der Wall: *Calculation of Multibladed Rotors in High-Speed Forward Flight with Weak Fluid-Structure-Interaction*, 27^{th} European Rotorcraft Forum, 11-14 September 2001, Moscow, Russia.

[4] H. Pomin, S. Wagner: *Navier-Stokes Analysis of Helicopter Rotor Aerodynamics in Hover and Forward Flight*, AIAA Paper 2001-0998.

[5] H. Pomin, S. Wagner: *Aeroelastic Analysis of Helicopter Rotor Blades on Deformable Chimera Grids*, AIAA Paper 2002-0951.

[6] H. v. Geyr, N. Kroll: *Application of 3D-Preconditioning for the Prediction of Helicopter Fuselage Drag Considering Interferences with Model Support Strut*, 25^{th} European Rotorcraft Forum, 14-16 September 1999, Rome, Italy.

[7] R. E. Mineck: *Application of an Unstructured Grid Navier-Stokes Solver to a Generic Helicopter Body - Comparison of Unstructured Grid Results with Structured Grid Results and Experimental Results*. NASA Report number: NASA/TM-1999-209510 Date: August 1999

[8] M. S. Chaffin, J. D. Berry: *Navier-Stokes and Potential Theory Solutions for a Helicopter Fuselage and Comparison With Experiment* NASA Report number(s): NASA TM-4566 ATCOM-TR-94-A-013

[9] W. Khier, F. le Chuiton, T. Schwarz : *Navier-Stokes Analysis of the Helicopter Rotor-Fuselage Interference in Forward Flight*, CEAS Aerospace Aerodynamics Research Conference, 10-12 June 2002, Cambridge, England.

[10] T. Schwarz: *Berechnung der Umstroemung einer Hubschrauber-Rotor-Rumpf-Konfiguration auf der Basis der Euler-Gleichungen mit der Chimaeren-Technik*, DLR Internal Report IB-NR 129-97/23.

[11] J. Brezillon: *Simulation of Rotor-Fuselage Interactions by using an Actuator disc* 26th European Rotorcraft Forum, The Hague, The Netherlands, 26-29 September 2000.

[12] B. S. Baldwin, H. Lomax: *Thin Layeer Approximation and Algebraic Model for Separated Turbulent Flows*, *AIAA paper*, 78-0257, 1978.

[13] P. R. Spalart, S. R. Allmaras: *A One-Equation Turbulence Model for Aerodynamic Flows*, *AIAA paper*, 92-439, 1992

[14] D. C. Wilcox: *Reassessment of the Scale-Determining Equation for Advanced Turbulence Models*, AIAA Journal, vol. 26, no. 11, November 1988.

[15] T. Rung, H. Lübcke, M. Franke, L. Xue, F. Thiele, S. Fu: *Assessement of Explicit Algebraic Stress Models in Transonic Flows*, 4^{th} Int. Symp. Engineering Turbulence Modelling and Measurements, Corsica, France 1999. pp. 659 - 668.

[16] F. R. Menter: *Two-Equation Eddy Viscosity Turbulence Models for Engineering Applications*, AIAA Journal, 32(8) (1994) 1598 - 1605.

[17] V. Mikulla: *Improved Experimental and Theoretical Tools for Helicopter Aeromechanic and Aeroacustic Interactions (HELIFLOW)*, Report No.: HFLOW/3/ECD/01, 1997.

[18] H. J. Langer, R. L. Peterson, T. H. Maier:*An Experimental Evaluation of Wind Tunnel Wall Correction Methods for Helicopter Performance*, American Helicopter Society 52^{nd} Annual Forum, Washington, D.C., June 4-6, 1996.

[19] B. Junker, H. J. Langer: *Private communication*

[20] W. R. Splettstoesser, B. Junker, K.-J. Schultz, W. Wagner, W. Weitemeyer, A. Protopsaltis, D. Fertis: *The HELINOISE Aeroacoustic Rotor Test in the DNW - Test Documentation and Representative Results*, DLR-Mitteilung 93-09.

[21] K. H. Ng, D. B.Spalding: *Some Applications of a Model of Turbulence for Boundary Layers Near Walls*, Mech. Eng. Dept. Imperial College. Rep. BL/TN/A/14, 1969.

[22] W. Rodi, D. B. Spalding: *A Two-Parameter Model of Turbulence and Its Application to Free Jets*, Wärme und Stoffübertragung, 3, 85-95, 1970.

[23] F. H. Harlow, P. I. Nakayama: *Transport of Turbulence Energy Decay Rate*, Los Alamos Sci. Lab. University of California Rep. LA 3854, 1968.

[24] W. P. Jones, B. E. Launder: *The Prediction of Laminarization with a 2-Equation Model of Turbulence*, Int. J. Heat. Mass Transfer, **15**, 301, 1972.

[25] J. A. Benek, J. L. Steger, F. C. Dougherty: *A Flexible Grid Embedding Technique with Aplication to the Euler Equations*, AIAA Paper 83-1944.

[26] T. Schwarz: *Development of a Wall Treatment for Navier-Stokes Computations using the Overset-Grid Technique*, 26th European Rotorcraft Forum, The Hague, The Netherlands, 26-29 September 2000.

[27] J. Bonet, J. Peraire: *An Alternating Digital Tree (ADT) Algorithm for 3D Geometric Searching an Intersection Problems*, International Journal for Numerical Problems in Engineering, vol. 31, 1-17, 1991.

[28] N. Kroll, C.-C. Rossow, K. Becker, F. Thiele:*The MEGAFLOW project*, Aerospace, Science and Technology, Vol. 4, pp. 223-237, 2000.

[29] A. Jameson, W. Schmidt, E. Turkel: *Numerical Solutions of the Euler Equations by Finite Volume Methods using Runge-Kutta Time-Stepping Schemes*, AIAA-Paper 81-1259, 1981.

[30] R. L. Meakin: *Moving Body Overset Grid Methods for Complete Aircraft Tiltrotor Simulations*, AIAA Paper 93-3350

[31] R. L. Meakin: *An Efficient Means of Adaptive Refinement Within Systems of Overset Grids* AIAA Paper 95-1722-CP, 12th AIAA Computational Fluid Dynamics Conference, San Diego, CA, June 1995 24-28 June 1996

[32] D. L. Rigby: *Method of Weakest Descent for Automatic Block Merging* Proceedings of the 15th International Conference on Numerical Methods in Fluid Dynamics, Monterey, CA, USA, 24-28 June 1996

[33] M. J. Aftosmis: *Solution Adaptive Cartesian Grid Methods for Aerodynamic Flows with Complex Geometries* 28th Computational Fluid Dynamics Lecture Series, von Karman Institute for Fluid Dynamics, Lecture Series 1997-02, 1997

[34] F. Deister, E. H. Hirschel: *Adaptive Cartesian/Prism Grid Generation and Solution for Arbitrary Geometries* 37th AIAA Aerocpace Sciences Meeting and Exhibit., Reno, NV, Jan 11-14, 1999